How the Bio-Inspired $Fe_2Mo_6S_8$ Chevrel Breaks Electrocatalytic Nitrogen Reduction Scaling Relations

Nicholas R. Singstock[1] and Charles B. Musgrave*[1,2,3]

[1]Department of Chemical and Biological Engineering, University of Colorado Boulder, Boulder, CO 80303, USA

[2]Materials Science and Engineering Program, University of Colorado Boulder, Boulder, CO 80303, USA

[3]Renewable and Sustainable Energy Institute, University of Colorado Boulder, Boulder, CO 80303, USA

KEYWORDS: Nitrogen Reduction, Chevrel Phase, Electrocatalysis, Grand-Canonical DFT

ABSTRACT: The nitrogen reduction reaction (NRR) is a renewable alternative to the energy and CO_2 intensive Haber-Bosch NH_3 synthesis process but is severely limited by the low activity and selectivity of studied electrocatalysts. The Chevrel phase $Fe_2Mo_6S_8$ has a surface Fe-S-Mo coordination environment that mimics the nitrogenase FeMo-cofactor and was recently shown to provide state-of-the-art activity and selectivity for NRR. Here, we unravel the previously-unknown NRR mechanism on $Fe_2Mo_6S_8$ via grand-canonical density functional theory (GC-DFT) that realistically models solvated and biased surfaces. Furthermore, we developed a new GC-DFT-based approach for calculating transition states (TS) as a function of bias (GC-NEB) and applied GC-NEB to develop a microkinetic model for NRR at $Fe_2Mo_6S_8$. Our results demonstrate that NRR occurs rapidly and selectively at Fe sites due to low TS barriers for both key reaction steps, which breaks conventional scaling relations. Fe sites selectively stabilize the key $*N_2$ protonation step via dissociation of a subsurface Fe-S bond that results in narrow bands of free-atom-like *d*-states that selectively hybridize with *p*-states of *NNH. Our results provide new design principles for effective NRR electrocatalysts and may be broadly applied to the rational discovery of stable, multinary electrocatalysts for other reactions where narrow bands of surface *d*-states can be tuned to selectively stabilize key reaction intermediates and guide selectivity towards a target product. Furthermore, our results highlight the importance of using GC-DFT and GC-NEB to accurately model electrocatalytic reactions.

INTRODUCTION

The synthesis of ammonia from nitrogen is a foundation of modern society due to the critical role it plays in producing ammonia for fertilizers that support feeding nearly half of the global population.[1,2] Over 90% of the world's 235 Mt/year production of NH_3 is generated via the Haber-Bosch process, which is highly energy intensive and generates ~1.8% of global CO_2 emissions annually.[3–9] Synthesis of NH_3 via the electrocatalytic nitrogen reduction reaction (NRR) is a promising alternative process because it can be powered by renewable electricity, uses N_2 and H_2O as sustainable inputs and enables distributed production.[4,7,8,10,11] Ammonia produced by NRR is also a promising fuel for renewable energy storage and a renewable precursor to other industrial chemicals such as nitric acid.[2,12] Yet, the development of NRR has been limited by the absence of an active and selective electrocatalyst, with the majority of currently studied materials yielding Faradaic efficiencies (FE) of <10% due to competition with proton reduction via the hydrogen evolution reaction (HER).[4,6,7,13–20] Furthermore, NRR activity and selectivity on transition-metal surfaces is severely limited by linear scaling relations between NRR intermediates, where metals with weaker nitrogen binding are limited by poor N_2 adsorption and high barriers for $*N_2$ protonation to *NNH, whereas metals with strong nitrogen binding are limited by high barriers for $*NH_3$ desorption (* denotes adsorbed species).[21]

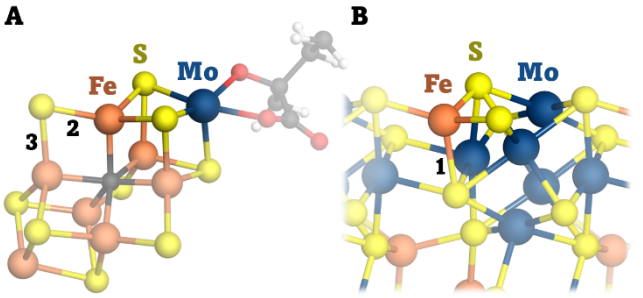


Figure 1: Structural Similarities of Fe-S-Mo Bonding. Ground-state structures of the nitrogenase FeMo-cofactor **(A)** and (110) $Fe_2Mo_6S_8$ Chevrel phase surface **(B)**. The similar Fe-S-Mo coordination of the structures is highlighted.

In nature, NH_3 is synthesized from N_2 by nitrogenase enzymes in conjunction with a catalytic FeMo-cofactor.[22–24] The impressive activity of the cofactor is enabled by its structure, which is comprised of Fe active sites coordinated with Mo through sulfur atoms (**Figure 1a**). An analogous inorganic structure is the metallic Chevrel phase $Fe_2Mo_6S_8$, where Fe atoms coordinate to an Mo_6 octahedra through sulfur atoms (**Figure 1b**). The Fe-S-Mo coordination environment of the

(110) surface of $Fe_2Mo_6S_8$ closely resembles that of the Fe active site of the FeMo-cofactor and may therefore provide favorable energetics for ambient conversion of N_2 to NH_3. Furthermore, during the preparation of this report, an experimental investigation of $Fe_2Mo_6S_8$ catalyzed NRR found that it yielded a state-of-the-art FE of 12.5% and a high rate of 70 μg NH_3 h^{-1} mg_{cat}^{-1} at a low bias of -0.20 V vs. RHE, which was stable over 50 h.[25] However, the mechanism for NRR on this impressive material has not yet been determined, limiting the understanding necessary to rationally design superior electrocatalysts in this material space.

To probe the NRR reaction mechanism on $Fe_2Mo_6S_8$ under realistic reaction conditions (e.g., in solvent with applied bias), we used grand-canonical density functional theory (GC-DFT)[26–28] and implemented a new GC-DFT approach to calculate reaction barriers as a function of the applied bias (GC-NEB, see **Methods**). We find that Fe surface sites on $Fe_2Mo_6S_8$ facilitate rapid NRR rates (>10 μg h^{-1} cm^{-2}) due to selective stabilization of the key *NNH intermediate relative to $*N_2$. Consequently, GC-NEB computes low barriers for both $*N_2$ protonation to *NNH and $*NH_3$ desorption, which are the rate determining steps (RDS) for metals with weaker and stronger nitrogen binding, respectively.[4,21] N_2 adsorption at Fe sites results in a concomitant dissociation of the subsurface Fe-S bond (1 in **Figure 1**), similar to the N_2 reduction mechanism on the nitrogenase FeMo- and FeV-cofactors where two Fe-S bonds dissociate (2 and 3 in **Figure 1**) to reveal the Fe active sites.[17,22,29] On $Fe_2Mo_6S_8$, this yields a trigonal pyramidal Fe active site with narrow bands of free-atom-like *d*-states that overlap significantly with the nitrogen *p*-states of *NNH, but not $*N_2$ or $*NH_3$, which selectively stabilizes *NNH and breaks conventional NRR scaling relations. The elucidation of the NRR mechanism on $Fe_2Mo_6S_8$ provides important insights into the rational design of superior electrocatalysts with high NH_3 activity and selectivity.

RESULTS AND DISCUSSION

NRR Mechanism on $Fe_2Mo_6S_8$

NRR involves the transfer of six protons and six electrons to N_2 to yield two NH_3 molecules. In electrocatalytic NRR, the protons and electrons are derived from water oxidation at the anode and are transferred to the $*N_xH_y$ species from the solvent and NRR electrocatalyst, respectively. Three reaction mechanisms have been proposed for NRR: 1) the associative alternating pathway, where the nitrogen atoms of $*N_2$ are protonated in parallel to form $*NH_2NH_2$ and then $*NH_3$ (**Figure 2**, opaque), 2) the associative distal pathway, where the nitrogen atoms are protonated in series to form $*NNH_3$ then $*NH_3$ (**Figure 2**, transparent), and 3) the dissociative pathway, where N_2 dissociatively adsorbs into two *N atoms at separate sites, which are subsequently protonated.[4,17,18] The dissociative pathway is not considered further due to the large change in grand-free energy (ΔΦ) for dissociative N_2 adsorption, which ranges from 2.81 to 2.44 eV at 0.0 V and -0.5 V, respectively (see **Figure S1**). For the associative pathways, NRR catalyzed by conventional metal surfaces is limited by the linear scaling of NRR intermediates, where metals with weaker N_2 binding are limited by $*N_2$ protonation to *NNH, and metals with stronger N_2 binding are limited by $*NH_3$ desorption.[17,21]

Chevrel phase $Fe_2Mo_6S_8$ is a multi-site catalyst with Mo, Fe and S surface sites that bind nitrogen and hydrogen. **Figures 2a** and **b** show the GC-DFT computed energies for the associative NRR pathways on Mo and Fe surface sites, respectively, from 0.0 to -0.5 V, which spans the range of commonly studied reducing biases.[6,15,25] Nitrogen and hydrogen binding is not favorable at S sites (**Figure S2**), while at Mo sites, NRR proceeds via either the associative alternating or associative distal pathways (**Figure 2a**). However, the final reaction step of both pathways is $*NH_3$ desorption, which requires a large desorption grand-free energy $\Delta\Phi_2$ of 1.16–1.32 eV at the considered biases. Consequently, the rate of NH_3 production (r_{NH3}) from Mo sites between 0.0 and -0.5 V is negligibly low, with $r_{NH3} < 4.4\times10^{-5}$ μg NH_3 h^{-1} cm^{-2} (i.e., 4.2×10^{-7} mA cm^{-2}) and a $*NH_3$ coverage > 99.999% if no additional activation barriers exist that would further lower NRR activity (i.e., $TS_2 \geq \Delta\Phi_2$). Consequently, our calculations predict that Mo sites are poisoned by over-binding of $*NH_3$, which results in negligible NRR and HER

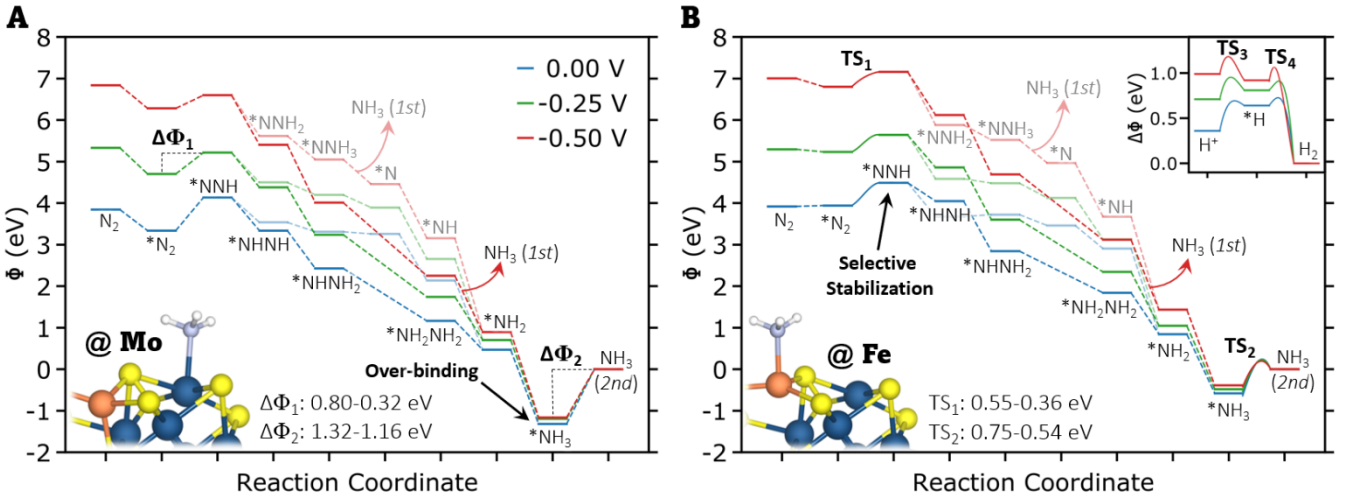


Figure 2: NRR Mechanism on $Fe_2Mo_6S_8$. The associative alternating (opaque) and associative distal (transparent) NRR pathways at Mo **(A)** and Fe **(B)** surface sites, at applied biases of 0.0, -0.25 and -0.5 V vs. RHE (red, green, blue, respectively) in H_2O solvent at pH 7. The Volmer-Heyrovsky HER pathway on Fe sites is shown in the inset. Transition states are included for $*N_2$ protonation (TS_1), $*NH_3$ desorption (TS_2), H^+ adsorption (TS_3) and *H protonation (TS_4) on Fe sites. NH_3(aq) is set as the grand-free energy (Φ) reference, which results in the bias dependence of the initial state.

activity at these sites at biases between 0.0 to -0.5 V (**Figure S3**).

NRR at Fe sites may also proceed through either associative pathway (**Figure 2b**), which both involve the same key reaction steps: $*N_2$ protonation to *NNH and $*NH_3$ desorption. Relative to binding at Mo sites, N_2 and NH_3 binding energies are shifted by +0.53 and +0.66 eV at 0 V, respectively. This suggests that Fe sites bind NRR intermediates more weakly than Mo sites. However, the reaction intermediate *NNH has a similar binding energy on both Fe and Mo sites (-0.03 and +0.06 eV at 0 V, respectively), indicating that Fe sites selectively stabilize the key *NNH intermediate relative to $*N_2$, which lowers the grand-free energy of $*N_2$ protonation, $\Delta\Phi_1$. Consequently $\Delta\Phi_1$ and $\Delta\Phi_2$ are both lower on Fe sites than on Mo sites. Furthermore, the $\Delta\Phi$ for these steps is not affected by $*NH_3$ adsorption at neighboring Mo sites (**Figure S4**). This selective stabilization of *NNH indicates that the Fe surface sites of $Fe_2Mo_6S_8$ break linear scaling relations for NRR.

Grand Canonical Microkinetic Modeling

To compute the kinetics of $Fe_2Mo_6S_8$ catalyzed NRR, we developed and applied a grand canonical implementation of the nudged elastic band method (GC-NEB, see **Methods**) to calculate the activation energies (Φ_a) for four key transition states (TSs) on Fe sites: 1) $*N_2$ protonation by H_3O^+ to form *NNH and H_2O (TS_1), 2) $*NH_3$ desorption (TS_2), 3) proton adsorption from H_3O^+ to form H* and H_2O (HER, Volmer step, TS_3), and 4) H* protonation by H_3O^+ to form H_2 and H_2O (HER, Heyrovsky step, TS_4). The TS grand-free energies are shown in **Figure 2b** as a function of bias. TS_1 has a low Φ_a at all three biases, decreasing from 0.55 to 0.36 eV as the bias decreases from 0.0 to -0.5 V, resulting in a large rate constant (k) of $>1.9\times10^4$ M^{-1} s^{-1}. $*NH_3$ desorbs reductively, requiring ~0.40 electrons to be transferred to the desorbing NH_3. Consequently, TS_2 is bias-dependent, with an Φ_a that decreases from 0.75 eV at 0.0 V to 0.54 eV at -0.5 V. This results in an increase in k from 8.1 to 2.9×10^4 s^{-1}. Thus, NRR at the Fe sites of $Fe_2Mo_6S_8$ proceeds via low Φ_a's for both TS_1 and TS_2 due to the selective stabilization of *NNH and the intermediate binding energy of $*NH_3$. The RDS between 0.0 and -0.5 V is TS_2. Non-GC approaches such as the computational hydrogen electrode (CHE) would fail to capture the bias-dependence of the RDS because it is not a proton-coupled electron transfer. GC-NEB was also used to compute the Φ_a's of the Volmer-Heyrovsky mechanism for HER at Fe sites to determine the activity of this reaction and the resultant selectivity towards NRR. At 0.0 V, both the Volmer ($H^+ \rightarrow H^*$) and Heyrovsky ($H^+ + H^* \rightarrow H_2$) steps have low Φ_a's of 0.34 and 0.09 eV, respectively, with the Volmer step being rate limiting. At more reducing biases, the Volmer barrier decreases and the Heyrovsky barrier slightly increases, shifting to 0.23 and 0.11 eV, respectively, at -0.5 V.

We developed a microkinetic model for NRR and HER on $Fe_2Mo_6S_8$ using the computed thermodynamics and Φ_a's of each reaction step (see **Methods** and **Section S2**). Mo sites have a negligible contribution to the current densities of NRR and HER (**Figure S3**). The low Φ_a's for both $*N_2$ protonation and $*NH_3$ desorption at Fe sites result in high selectivity towards NRR, with a FE of 74-99% at pH 7 (**Figure 3a**). However, at pH 7 the activity of NRR is low due to the low $[H^+]$, with a current density of only 2.1×10^{-3} mA cm^{-2} at -0.5 V. Decreasing the solvent pH increases NRR activity, however it also increases HER activity at a greater rate, resulting in a decrease of FE as the pH decreases below 7. This effect is evident in **Figure 3b**, where the NH_3 yield is maximized at lower pH and more reducing biases, but the FE is maximized at higher pH and less reducing biases. **Figure 3b** further demonstrates the challenge of identifying superior NRR electrocatalysts with desirable metrics for both activity and selectivity, which are maximized under different conditions. Despite this limitation, the pH range of 5-6 combined with a bias of -0.5 V balances a high FE (9-26%) and a high NH_3 yield (39-392 μg h^{-1} mg_{cat}^{-1} and 0.02-0.2 mA cm^{-2}), which is superior to most NRR electrocatalysts studied to-date.[6,11,13] These results are in good agreement with recent experimental metrics of 12.5% FE and 70 μg NH_3 h^{-1} mg_{cat}^{-1} at pH 4.5 and -0.2 V,[25] despite the exponential sensitivity of NRR activity and selectivity on reactor conditions. Our model predicts 6.0% FE and 1.7 μg NH_3 h^{-1} mg_{cat}^{-1} at pH 4.5 and -0.2 V.

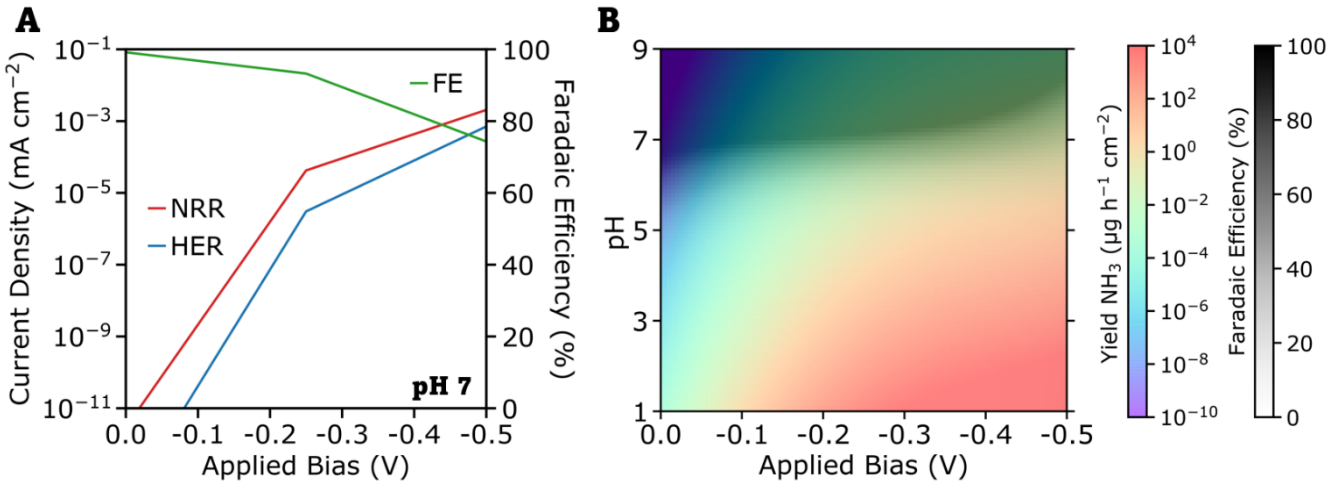


Figure 3: NRR Microkinetic Model. Current densities for NRR and HER, and NRR Faradaic efficiency **(A)** calculated at biases of 0.0, -0.25 and -0.5 V at pH 7 using an NRR microkinetic model based on reaction barriers computed by GC-NEB. **(B)** Heatmap of NH_3 yield (color) and NRR FE (black & white shading) as pH and applied bias are varied in the NRR microkinetic model for $Fe_2Mo_6S_8$. Both Fe and Mo sites are considered in the microkinetic model.

We also developed a simplified microkinetic model based on energies calculated with the CHE approximation[27] (**Figure S5**), which deviates considerably from experiment (e.g., 0.5% FE and 0.008 μg NH_3 h^{-1} mg_{cat}^{-1} at pH 5 and -0.25 V) and underscores the need for GC-DFT and GC-NEB to accurately model electrochemical NRR.

How Fe Sites Break Linear Scaling

The impressive activity and selectivity of the Fe surface sites of $Fe_2Mo_6S_8$ is a consequence of their selective stabilization of *NNH relative to $*N_2$ and $*NH_3$. During N_2 adsorption on Fe, a concurrent dissociation of the subsurface Fe-S bond occurs to stabilize the Fe-N bond (see **Figures 4a** and **b**), enabling an S_N2 reaction for this step to activate the N_2 triple-bond. This is similar to the N_2 reduction mechanism of the nitrogenase FeMo- and FeV-cofactors where two Fe-S bonds (2 and 3 in **Figure 1**) dissociate to produce the trigonal pyramidal Fe active site.[17,22,29] Fe-S subsurface bond dissociation on $Fe_2Mo_6S_8$ also yields a trigonal pyramidal active site (tetrahedral with $*N_xH_y$). This mechanism supports the biomimetic properties of $Fe_2Mo_6S_8$. The Fe-S subsurface bond remains broken until $*NH_3$ desorbs (**Figure 4d**). In contrast, the Fe-S bond remains intact upon proton adsorption at Fe sites.

An intriguing consequence of the subsurface Fe-S bond dissociation and the rearrangement of the Fe site geometry is the narrowing of the d_{z^2} band of the surface Fe atom into free-atom-like states at -6.5 and -3.8 eV below the Fermi level. Narrow *d*-state bands in single-atom catalysts have been shown to influence selectivity via hybridization with molecular orbitals of a similar energy, which selectively stabilizes the corresponding adsorbates.[30] The bonding d_{z^2} state at -6.5 eV exhibits significant overlap with the p_y state of the bound N of *NNH (**Figure 4c**), however minimal overlap exists between these states in $*N_2$ and $*NH_3$ (**Figures 4b** and **d**). The large and selective overlap between the Fe d_{z^2} and *NNH p_y states indicates a selective stabilization of *NNH relative to $*N_2$ or $*NH_3$, matching the calculated binding energies of these adsorbates. Additionally, we fixed the Fe surface atom in our model to its position in the clean surface, and then adsorbed $*N_2$, *NNH and $*NH_3$ to the fixed Fe atom to determine the importance of the Fe-S bond dissociation on the binding energies of these adsorbates. This prevents the Fe-S bond from dissociating and the band of surface *d*-states from narrowing (**Figure 4e**). Consequently, no selective stabilization of *NNH is calculated when the Fe surface atom is fixed, and the ΔΦ for $*N_2$ protonation to *NNH is 1.19 eV at -0.5 V, vs. 0.36 eV when the surface Fe atom is free to dissociate from the subsurface S atom.

In contrast to $Fe_2Mo_6S_8$, the measured FE and activity of NRR catalyzed by the $Cu_2Mo_6S_8$ Chevrel phase are an order of magnitude lower than that of $Fe_2Mo_6S_8$,[25] despite its similar structure, composition and bulk electronic properties.[31,32] The Cu surface sites of $Cu_2Mo_6S_8$ bind more weakly to $*N_2$ and $*NH_3$ (see **Figure 4f**), and do not selectively stabilize *NNH. This significantly increases the ΔΦ of $*N_2$ protonation to 1.06-1.36 eV between 0.0 and -0.5 V vs. 0.36-0.55 eV on $Fe_2Mo_6S_8$, which dramatically decreases the calculated NRR activity of Cu sites to $<1.0\times10^{-8}$ μg h^{-1} cm^{-2} at all conditions (**Figure S6**). Analogous to $Fe_2Mo_6S_8$, *NNH binding at Cu surface sites of $Cu_2Mo_6S_8$ causes a dissociation of the subsurface Cu-S bond. However, the Cu atom only shifts 0.54 Å in the z-direction vs. a 0.76 Å shift of Fe in $Fe_2Mo_6S_8$. Consequently, the band of d_{z^2} states of the surface Cu atom does not narrow, and this broad band of *d*-states overlap minimally with the N p_y states of *NNH (**Figures 4g** and **h**). Thus, the negligible overlap of surface d_{z^2} states with the *NNH p_y states at Cu sites produces conventional scaling limitations of NRR intermediates on $Cu_2Mo_6S_8$, and ultimately low NRR activity

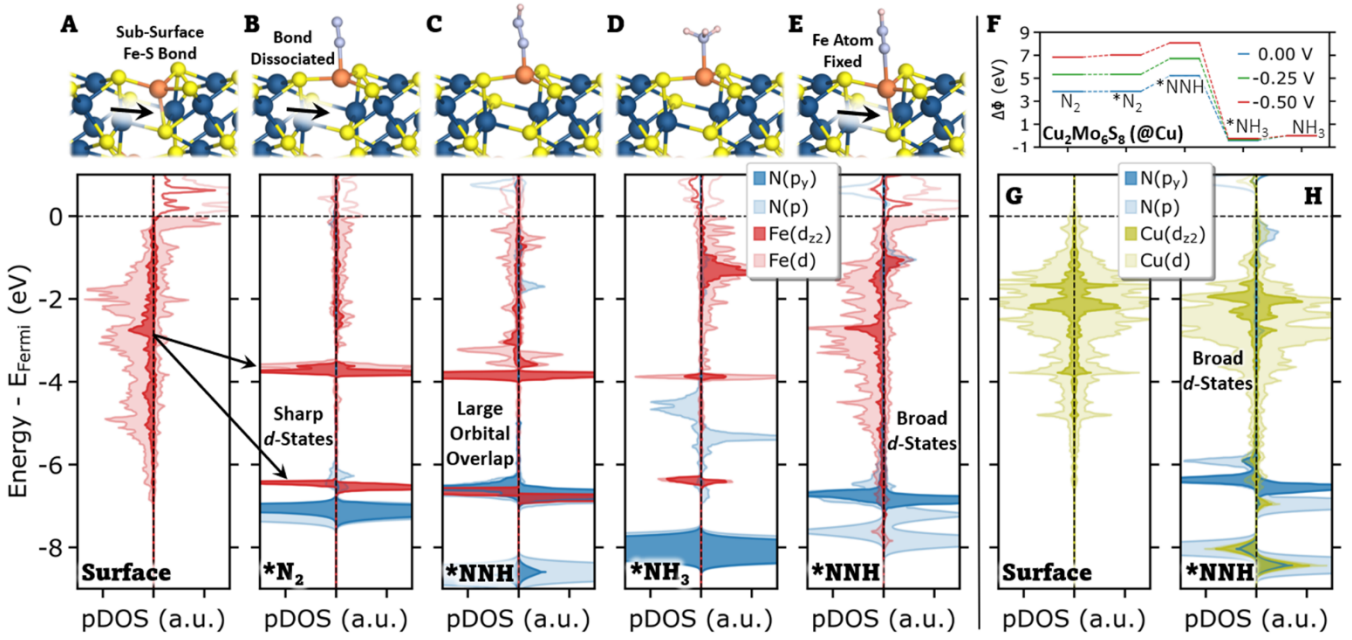


Figure 4: Selective *NNH Stabilization. Structure and projected density of states (pDOS) for the clean $Fe_2Mo_6S_8$ surface **(A)**, and the $Fe_2Mo_6S_8$ surface with $*N_2$ **(B)**, *NNH **(C)**, $*NH_3$ **(D)**, and *NNH with the Fe surface atom fixed at its position on the clean surface **(E)**. The abbreviated NRR mechanism on $Cu_2Mo_6S_8$ **(F)** is included for comparison alongside the pDOS of the clean **(G)** and *NNH covered **(H)** $Cu_2Mo_6S_8$ surfaces. The pDOS for these structures is shown for the surface Fe/Cu atom and adsorbed *N atom, at 0.0 V.

and selectivity (**Figure S6**).

Our results show that superior NRR activity and selectivity may be achieved by materials that selectively stabilize *NNH relative to $*N_2$, while binding $*NH_3$ more weakly than $Fe_2Mo_6S_8$. New materials can be rapidly screened by their free energies to protonate $*N_2$ to *NNH and desorb $*NH_3$ to identify promising candidates that minimize the Φ_a barriers of both of these key reaction steps. We thus recommend high-throughput screening of multinary materials with Fe-C-TM (C=chalcogenide; TM=redox-active transition metal) coordination environments to identify superior NRR electrocatalysts with low $\Delta\Phi$ and Φ_a of $*N_2$ protonation and $*NH_3$ desorption. The multinary Chevrel phases may provide an ideal platform for designing electrocatalysts that meet these criteria due to the similarity of their active sites to the nitrogenase co-factors and their tunable compositions that allow a range of chalcogenide stoichiometries and transition-metal intercalants.[33–35] Expanding the set of NRR electrocatalysts that break scaling relations via GC-DFT studies may elucidate the importance of narrow bands of surface *d*-states near -6.5 eV below the Fermi level, concurrent N_2 adsorption and Fe-S bond dissociation, and the trigonal pyramidal Fe active site geometry (tetrahedral with $*N_xH_y$).

CONCLUSION

$Fe_2Mo_6S_8$ provides state-of-the-art activity and selectivity for NRR via the selective stabilization of *NNH relative to $*N_2$ that results in low Φ_a's for the key NRR reaction steps of $*N_2$ protonation and $*NH_3$ desorption. This selective stabilization results from the narrow band of free-atom-like *d*-states that arise via a biomimetic Fe-S bond dissociation during NRR. New materials can be screened by their $\Delta\Phi$'s of $*N_2$ protonation and $*NH_3$ desorption to identify promising NRR electrocatalysts that break scaling relations, analogous to $Fe_2Mo_6S_8$. Our results also highlight the need for a grand-canonical approach for modeling electrocatalytic systems, which is necessary to illuminate the bias-dependence of the RDS at Fe surface sites and to accurately predict NRR activity and selectivity. We anticipate that grand-canonical modeling, including GC-NEB, will be critical for developing realistic and accurate mechanisms and microkinetic models for other electrochemical reactions. Furthermore, the mechanism discovered here provides new insights for designing stable, multinary electrocatalysts for other reactions, where the energy levels of narrow bands of surface *d*-states may be tuned to selectively hybridize with key reaction intermediates, resulting in improved activity and/or selectivity towards a target product. A rational electrocatalyst design platform may be developed by compositionally tuning the Chevrel phases.

EXPERIMENTAL SECTION

GC-DFT

GC-DFT calculations were performed using the JDFTx software.[36,37] All calculations were performed using the PBE functional,[38] with the D2 van der Waals correction.[39] General calculation parameters included a 20 Hartree electronic energy cutoff, spin polarization, no symmetry constraints, a Γ-centered k-point grid with a density of $1000/N_{atoms}$, and an energy convergence threshold of 1 meV. Calculations of surfaces and adsorbate systems were performed using the CANDLE linear PCM solvation model for H_2O, with 0.5 M Na^+ and F^- ions.[26,40] A more complete description of the methods used to calculate and generate reaction pathways (**Figure 2**) is provided in **Section S1**.

All reaction pathways were shifted so that the final state -- $2NH_3$ or H_2 -- was defined as having a grand-free energy of 0 eV. This shifts the initial state -- N_2 and 6 protons for NRR, 2 protons for HER -- as the bias becomes more reducing due to the relative destabilization (stabilization) of protons (electrons) in the solvent (bulk electrode). This represents the system more accurately than setting the initial state of the reaction pathway as the reference, which implies that the neutral product molecules NH_3 and H_2 are stabilized by a more reducing bias. Additional discussion of reference states is available in **Section S1**.

Orbital-projected density of states (pDOS) were calculated for specific surface and adsorbate systems using JDFTx. Calculated pDOS were plotted with a Gaussian smearing of 0.1 eV using Pymatgen,[41] and were centered to the Fermi level.

Grand-Canonical Nudged Elastic Band Approach

We implemented the GC-NEB approach to calculate TS pathways as a function of bias, while allowing the fractional transfer of electrons between the surface and adsorbate throughout the TS pathway. GC-NEB is only the second implementation of a fully grand-canonical approach for relaxing TS pathways in equilibrium with an applied bias.[42] We improved the base JDFTx calculator in the pythonic atomic simulation environment (ASE),[43] to enable its use with the ASE implementation of the NEB method.[44,45] This allowed each NEB image to be calculated with JDFTx at the corresponding bias with an independent charge density and solvent response. GC-NEB calculation parameters are readily switched between a variety of different solvent models, biases, NEB optimizers, TS images, DFT functionals, etc., and this code can be readily applied to any surface calculations. The GC-NEB code is available at https://github.com/Nick-Singstock/GCNEB and contains a detailed description and tutorials to setup and run GC-DFT and GC-NEB calculations.

In this work we used five NEB images (not including the initial and final states) to calculate the TS pathways and E_a. E_a is calculated as the difference between the maximum energy along the converged TS path and the energy of the initial state. For protonation reactions, an H_3O^+ molecule was placed above the atom being protonated, with a hydrogen atom pointing in the -z direction toward the surface, separated from the atom being protonated by 1.8 Å. The final state included both the protonated adsorbate and the remaining H_2O molecule above the surface.

Microkinetic Model

A microkinetic model was developed that includes NRR and HER steps to calculate the coverage of different adsorbates, the reaction rates of the elementary steps, the current density for NRR and HER, the mass yield of NH_3 and H_2, and the FE of NRR. Detailed descriptions of the calculations of elementary step rate constants, steady-state adsorbate coverages, and microkinetic model outputs are included in **Section S2**.

ASSOCIATED CONTENT

Additional figures and methods are available in the Supporting Information. This material is available free of charge via the Internet. Codes, data and tutorials are available for free at https://github.com/Nick-Singstock/GCNEB.

AUTHOR INFORMATION

Corresponding Author

* Charles B. Musgrave: charles.musgrave@colorado.edu

Author Contributions

NRS developed the GC-NEB implementation, ran all calculations, analyzed the data, created figures and drafted the manuscript. NRS and CBM conceived the project and reviewed and edited the manuscript.

Conflicts of Interest

The authors report no conflicts of interest.

ACKNOWLEDGMENT

NRS was supported by the National Science Foundation (awards CBET-1806079 and CBET-2016225). NRS and CBM also acknowledge support from the U.S. Department of Energy, Office of Science, Basic Energy Sciences (DE-SC0022247). This work utilized resources from the University of Colorado Boulder Research Computing Group, which is supported by the National Science Foundation (awards ACI-1532235 and ACI-1532236), the University of Colorado Boulder, and Colorado State University.

ABBREVIATIONS

NRR, nitrogen reduction reaction; HER, hydrogen evolution reaction; FE, Faradaic efficiency; GC-DFT, grand-canonical density functional theory; GC-NEB, grand-canonical nudged elastic band method; RDS, rate-determining step; TS, transition state; CHE, computational hydrogen electrode method.

REFERENCES

(1) Erisman, J. W.; Sutton, M. A.; Galloway, J.; Klimont, Z.; Winiwarter, W. How a Century of Ammonia Synthesis Changed the World. *Nat. Geosci.* **2008**, *1* (10), 636–639. https://doi.org/10.1038/ngeo325.

(2) Chen, J. G.; Crooks, R. M.; Seefeldt, L. C.; Bren, K. L.; Morris Bullock, R.; Darensbourg, M. Y.; Holland, P. L.; Hoffman, B.; Janik, M. J.; Jones, A. K.; et al. Beyond Fossil Fuel–Driven Nitrogen Transformations. *Science (80-.).* **2018**, *360* (6391). https://doi.org/10.1126/SCIENCE.AAR6611/ASSET/4CCE9F55-CFFD-4C23-8B70-1DE141F9256C/ASSETS/GRAPHIC/360_AAR6611_FA.JPEG.

(3) Han, G. F.; Li, F.; Chen, Z. W.; Coppex, C.; Kim, S. J.; Noh, H. J.; Fu, Z.; Lu, Y.; Singh, C. V.; Siahrostami, S.; et al. Mechanochemistry for Ammonia Synthesis under Mild Conditions. *Nat. Nanotechnol.* **2020**, *16* (3), 325–330. https://doi.org/10.1038/s41565-020-00809-9.

(4) Guo, C.; Ran, J.; Vasileff, A.; Qiao, S. Rational Design of Electrocatalysts and Photo(Electro)Catalysts for Nitrogen Reduction to Ammonia (NH3) under Ambient Conditions. *Energy Environ. Sci.* **2018**, *11* (1), 45–56. https://doi.org/10.1039/c7ee02220d.

(5) Humphreys, J.; Lan, R.; Tao, S. Development and Recent Progress on Ammonia Synthesis Catalysts for Haber–Bosch Process. *Adv. Energy Sustain. Res.* **2021**, *2* (1), 2000043. https://doi.org/10.1002/AESR.202000043.

(6) Cao, N.; Zheng, G. Aqueous Electrocatalytic N2 Reduction under Ambient Conditions. *Nano Res.* **2018**, *11* (6), 2992–3008. https://doi.org/10.1007/s12274-018-1987-y.

(7) Lim, J.; Fernández, C. A.; Lee, S. W.; Hatzell, M. C. Ammonia and Nitric Acid Demands for Fertilizer Use in 2050. *ACS Energy Lett.* **2021**, *6* (10), 3676–3685. https://doi.org/10.1021/ACSENERGYLETT.1C01614.

(8) Wang, L.; Xia, M.; Wang, H.; Huang, K.; Qian, C.; Maravelias, C. T.; Ozin, G. A. Greening Ammonia toward the Solar Ammonia Refinery. *Joule* **2018**, *2* (6), 1055–1074. https://doi.org/10.1016/J.JOULE.2018.04.017.

(9) David, B.; Bird, F.; Clarke, A.; Davies, P.; Surkovic, E. *Ammonia: Zero-Carbon Fertiliser, Fuel and Energy Store*; 2020.

(10) Suryanto, B.; Du, H.-L.; Wang, D.; Chen, J.; Simonov, A.; MacFarlane, D. Challenges and Prospects in the Catalysis of Electroreduction of Nitrogen to Ammonia. *Nat. Catal.* **2019**, *2* (4), 290–296. https://doi.org/10.1038/s41929-019-0252-4.

(11) Tang, C.; Qiao, S. Z. How to Explore Ambient Electrocatalytic Nitrogen Reduction Reliably and Insightfully. *Chem. Soc. Rev.* **2019**, *48* (12), 3166–3180. https://doi.org/10.1039/C9CS00280D.

(12) Service, R. F. Liquid Sunshine. *Science (80-.).* **2018**, *361* (6398), 120–123. https://doi.org/10.1126/SCIENCE.361.6398.120/ASSET/9D0DD2CA-E2BA-47EA-AED8-DBDABA76CF5A/ASSETS/GRAPHIC/361_120_F3.JPEG.

(13) Zhao, X.; Hu, G.; Chen, G. F.; Zhang, H.; Zhang, S.; Wang, H. Comprehensive Understanding of the Thriving Ambient Electrochemical Nitrogen Reduction Reaction. *Adv. Mater.* **2021**, *33* (33), 2007650. https://doi.org/10.1002/ADMA.202007650.

(14) Andersen, S. Z.; Čolić, V.; Yang, S.; Schwalbe, J. A.; Nielander, A. C.; McEnaney, J. M.; Enemark-Rasmussen, K.; Baker, J. G.; Singh, A. R.; Rohr, B. A.; et al. A Rigorous Electrochemical Ammonia Synthesis Protocol with Quantitative Isotope Measurements. *Nature* **2019**, *570* (7762), 504–508. https://doi.org/10.1038/s41586-019-1260-x.

(15) Li, W.; Li, K.; Ye, Y.; Zhang, S.; Liu, Y.; Wang, G.; Liang, C.; Zhang, H.; Zhao, H. Efficient Electrocatalytic Nitrogen Reduction to Ammonia with Aqueous Silver Nanodots. *Commun. Chem.* **2021**, *4* (1), 1–11. https://doi.org/10.1038/s42004-021-00449-7.

(16) Xu, H.; Ithisuphalap, K.; Li, Y.; Mukherjee, S.; Lattimer, J.; Soloveichik, G.; Wu, G. Electrochemical Ammonia Synthesis through N2 and H2O under Ambient Conditions: Theory, Practices, and Challenges for Catalysts and Electrolytes. *Nano Energy* **2020**, *69*, 104469. https://doi.org/10.1016/J.NANOEN.2020.104469.

(17) Foster, S. L.; Bakovic, S. I. P.; Duda, R. D.; Maheshwari, S.; Milton, R. D.; Minteer, S. D.; Janik, M. J.; Renner, J. N.; Greenlee, L. F. Catalysts for Nitrogen Reduction to Ammonia. *Nat. Catal.* **2018**, *1* (7), 490–500. https://doi.org/10.1038/s41929-018-0092-7.

(18) Zhang, L.; Ji, X.; Ren, X.; Ma, Y.; Shi, X.; Tian, Z.; Asiri, A. M.; Chen, L.; Tang, B.; Sun, X.; et al. Electrochemical Ammonia Synthesis via Nitrogen Reduction Reaction on a MoS2 Catalyst: Theoretical and Experimental Studies. *Adv. Mater.* **2018**, *30* (28), 1800191. https://doi.org/10.1002/ADMA.201800191.

(19) Jin, H.; Li, L.; Liu, X.; Tang, C.; Xu, W.; Chen, S.; Song, L.; Zheng, Y.; Qiao, S.-Z.; Jin, H.; et al. Nitrogen Vacancies on 2D Layered W2N3: A Stable and Efficient Active Site for Nitrogen Reduction Reaction. *Adv. Mater.* **2019**, *31* (32), 1902709. https://doi.org/10.1002/ADMA.201902709.

(20) Song, Y.; Johnson, D.; Peng, R.; Hensley, D. K.; Bonnesen, P. V.; Liang, L.; Huang, J.; Yang, F.; Zhang, F.; Qiao, R.; et al. A Physical Catalyst for the Electrolysis of Nitrogen to Ammonia. *Sci. Adv.* **2018**, *4* (4). https://doi.org/10.1126/SCIADV.1700336/SUPPL_FILE/1700336_SM.PDF.

(21) Montoya, J. H.; Tsai, C.; Vojvodic, A.; Nørskov, J. K. The

Challenge of Electrochemical Ammonia Synthesis: A New Perspective on the Role of Nitrogen Scaling Relations. *ChemSusChem* **2015**, *8* (13), 2180–2186. https://doi.org/10.1002/CSSC.201500322.

(22) Sippel, D.; Rohde, M.; Netzer, J.; Trncik, C.; Gies, J.; Grunau, K.; Djurdjevic, I.; Decamps, L.; Andrade, S. L. A.; Einsle, O. A Bound Reaction Intermediate Sheds Light on the Mechanism of Nitrogenase. *Science (80-.).* **2018**, *359* (6383), 1484–1489. https://doi.org/10.1126/SCIENCE.AAR2765/SUPPL_FILE/AAR2765_SIPPEL_SM.PDF.

(23) Čorić, I.; Mercado, B. Q.; Bill, E.; Vinyard, D. J.; Holland, P. L. Binding of Dinitrogen to an Iron–Sulfur–Carbon Site. *Nature* **2015**, *526* (7571), 96–99. https://doi.org/10.1038/nature15246.

(24) Lukoyanov, D. A.; Yang, Z.-Y.; Dean, D. R.; Seefeldt, L. C.; Raugei, S.; Hoffman, B. M. Electron Redistribution within the Nitrogenase Active Site FeMo-Cofactor During Reductive Elimination of H2 to Achieve N≡N Triple-Bond Activation. *J. Am. Chem. Soc.* **2020**, *142* (52), 21679–21690. https://doi.org/10.1021/JACS.0C07914.

(25) Lu, K.; Xia, F.; Li, B.; Liu, Y.; Razak, I. B. A.; Gao, S.; Kaelin, J.; Brown, D. E.; Cheng, Y. Synergistic Multisites Fe2Mo6S8 Electrocatalysts for Ambient Nitrogen Conversion to Ammonia. *ACS Nano* **2021**, acsnano.1c07771. https://doi.org/10.1021/ACSNANO.1C07771.

(26) Schwarz, K.; Sundararaman, R. The Electrochemical Interface in First-Principles Calculations. *Surface Science Reports*. Elsevier B.V. May 1, 2020, p 100492. https://doi.org/10.1016/j.surfrep.2020.100492.

(27) Alsunni, Y. A.; Alherz, A. W.; Musgrave, C. B. Electrocatalytic Reduction of CO2 to CO over Ag(110) and Cu(211) Modeled by Grand-Canonical Density Functional Theory. *J. Phys. Chem. C* **2021**, *125* (43), 23773–23783. https://doi.org/10.1021/acs.jpcc.1c07484.

(28) Liu, C.; Qian, J.; Ye, Y.; Zhou, H.; Sun, C. J.; Sheehan, C.; Zhang, Z.; Wan, G.; Liu, Y. S.; Guo, J.; et al. Oxygen Evolution Reaction over Catalytic Single-Site Co in a Well-Defined Brookite TiO2 Nanorod Surface. *Nat. Catal.* **2020**, *4* (1), 36–45. https://doi.org/10.1038/s41929-020-00550-5.

(29) Varley, J. B.; Wang, Y.; Chan, K.; Studt, F.; Nørskov, J. K. Mechanistic Insights into Nitrogen Fixation by Nitrogenase Enzymes. *Phys. Chem. Chem. Phys.* **2015**, *17* (44), 29541–29547. https://doi.org/10.1039/C5CP04034E.

(30) Spivey, T. D.; Holewinski, A. Selective Interactions between Free-Atom-like d-States in Single-Atom Alloy Catalysts and Near-Frontier Molecular Orbitals. *J. Am. Chem. Soc.* **2021**, *143* (31), 11897–11902. https://doi.org/10.1021/JACS.1C04234/SUPPL_FILE/JA1C04234_SI_001.PDF.

(31) Lilova, K.; Perryman, J. T.; Singstock, N. R.; Abramchuk, M.; Subramani, T.; Lam, A.; Yoo, R.; Ortiz-Rodríguez, J. C.; Musgrave, C. B.; Navrotsky, A.; et al. A Synergistic Approach to Unraveling the Thermodynamic Stability of Binary and Ternary Chevrel Phase Sulfides. *Chem. Mater.* **2020**, *32*, 46. https://doi.org/10.1021/acs.chemmater.0c02648.

(32) Perryman, J. T.; Hyler, F. P.; Ortiz-Rodríguez, J. C.; Mehta, A.; Kulkarni, A. R.; Velázquez, J. M. X-Ray Absorption Spectroscopy Study of the Electronic Structure and Local Coordination of 1st Row Transition Metal-Promoted Chevrel-Phase Sulfides. *J. Coord. Chem.* **2019**, *72* (8), 1322–1335. https://doi.org/10.1080/00958972.2019.1613532.

(33) Singstock, N. R.; Ortiz-Rodríguez, J. C.; Perryman, J. T.; Sutton, C.; Velázquez, J. M.; Musgrave, C. B. Machine Learning Guided Synthesis of Multinary Chevrel Phase Chalcogenides. *J. Am. Chem. Soc.* **2021**, *143* (24), 9113–9122. https://doi.org/10.1021/JACS.1C02971.

(34) Ortiz-Rodríguez, J. C.; Singstock, N. R.; Perryman, J. T.; Hyler, F. P.; Jones, S. J.; Holder, A. M.; Musgrave, C. B.; Velázquez, J. M. Stabilizing Hydrogen Adsorption through Theory-Guided Chalcogen Substitution in Chevrel-Phase Mo6X8 (X=S, Se, Te) Electrocatalysts. *ACS Appl. Mater. Interfaces* **2020**, *12* (32), 35995–36003. https://doi.org/10.1021/acsami.0c07207.

(35) Perryman, J. T.; Velázquez, J. M. Design Principles for Multinary Metal Chalcogenides: Toward Programmable Reactivity in Energy Conversion. *Chem. Mater.* **2021**, *33* (18), 7133–7147. https://doi.org/10.1021/ACS.CHEMMATER.1C01983.

(36) Sundararaman, R.; Letchworth-Weaver, K.; Schwarz, K. A.; Gunceler, D.; Ozhabes, Y.; Arias, T. A. JDFTx: Software for Joint Density-Functional Theory. *SoftwareX* **2017**, *6*, 278–284. https://doi.org/10.1016/j.softx.2017.10.006.

(37) Sundararaman, R.; Goddard, W. A.; Arias, T. A. Grand Canonical Electronic Density-Functional Theory: Algorithms and Applications to Electrochemistry. *J. Chem. Phys.* **2017**, *146* (11). https://doi.org/10.1063/1.4978411.

(38) Perdew, J. P.; Burke, K.; Ernzerhof, M. Generalized Gradient Approximation Made Simple. *Phys. Rev. Lett.* **1996**, *77* (18), 3865–3868.

(39) Grimme, S. Semiempirical GGA-Type Density Functional Constructed with a Long-Range Dispersion Correction. *J. Comput. Chem.* **2006**, *27* (15), 1787–1799. https://doi.org/10.1002/JCC.20495.

(40) Sundararaman, R.; Goddard, W. A. The Charge-Asymmetric Nonlocally Determined Local-Electric (CANDLE) Solvation Model. *J. Chem. Phys.* **2015**, *142* (6), 064107. https://doi.org/10.1063/1.4907731.

(41) Ong, S. P.; Richards, W. D.; Jain, A.; Hautier, G.; Kocher, M.; Cholia, S.; Gunter, D.; Chevrier, V. L.; Persson, K. A.; Ceder, G. Python Materials Genomics (Pymatgen): A Robust, Open-Source Python Library for Materials Analysis. *Comput. Mater. Sci.* **2013**, *68*, 314–319. https://doi.org/10.1016/j.commatsci.2012.10.028.

(42) Kastlunger, G.; Lindgren, P.; Peterson, A. A. Controlled-Potential Simulation of Elementary Electrochemical Reactions: Proton Discharge on Metal Surfaces. *J. Phys. Chem. C* **2018**, *122* (24), 12771–12781. https://doi.org/10.1021/acs.jpcc.8b02465.

(43) Larsen, A. H.; Mortensen, J. J.; Blomqvist, J.; Castelli, I. E.; Christensen, R.; Dułak, M.; Friis, J.; Groves, M. N.; Hammer, B.; Hargus, C.; et al. The Atomic Simulation Environment—a Python Library for Working with Atoms. *J. Phys. Condens. Matter* **2017**, *29* (27), 273002. https://doi.org/10.1088/1361-648X/AA680E.

(44) Mills, G.; Jónsson, H. Quantum and Thermal Effects in H2 Dissociative Adsorption: Evaluation of Free Energy Barriers in Multidimensional Quantum Systems. *Phys. Rev. Lett.* **1994**, *72* (7), 1124. https://doi.org/10.1103/PhysRevLett.72.1124.

(45) Henkelman, G.; Uberuaga, B. P.; Jónsson, H. A Climbing Image Nudged Elastic Band Method for Finding Saddle Points and Minimum Energy Paths. *J. Chem. Phys.* **2000**, *113* (22), 9901. https://doi.org/10.1063/1.1329672.

TABLE OF CONTENTS GRAPHIC

